

Majorana Kramers pair in a nematic vortex

Fengcheng Wu¹ and Ivar Martin¹

¹*Materials Science Division, Argonne National Laboratory, Argonne, IL 60439, USA*

(Dated: March 2, 2022)

A time-reversal (TR) invariant topological superconductor is characterized by a Kramers pair of Majorana zero-energy modes on boundaries and in a core of a TR invariant vortex. A vortex defect that preserves TR symmetry has remained primarily of theoretical interest, since typically a magnetic field, which explicitly breaks TR, needs to be applied to create vortices in superconductors. In this work, we show that an odd-parity topological superconductor with a nematic pairing order parameter can host a *nematic vortex* that preserves TR symmetry and binds a Majorana Kramers pair. Such a nematic superconductor could be realized in metal-doped Bi₂Se₃, as suggested by recent experiments. We provide an analytic solution for the zero modes in a continuous nematic vortex. In lattice, crystalline anisotropy can pin the two-component order parameter along high-symmetry directions. We show that a discrete nematic vortex, which forms when three nematic domains meet, also supports a TR pair of Majorana modes. Finally, we discuss possible experiments to probe the zero modes.

I. INTRODUCTION

Topological superconductors represent a paradigmatic system where topological effects and many-body interactions can have an interesting interplay. Topological superconductors with broken time reversal (TR) symmetry support Majorana zero-energy modes localized at the boundaries¹ and in the vortex cores^{2,3}. The non-Abelian statistics of Majorana modes may be utilized for fault-tolerant quantum computation⁴. The search for Majorana modes has been greatly influenced by the theoretical proposals based on topological insulator surface states⁵ or Rashba wires^{6,7} in proximity to ordinary *s*-wave superconductors in presence of magnetic field. Exciting experimental progress^{8,9} has been made along the lines of these proposals. When TR symmetry is preserved, the Kramers pairs of Majorana modes have been predicted to exist at the boundaries of some families of topological superconductors¹⁰. TR symmetric topological superconductors have been theoretically proposed to be realized, for example, in Cu_xBi₂Se₃¹¹ and in materials with strong spin-orbit coupling in proximity to π Josephson junction^{12,13} or *s*_±-wave superconductors¹⁴. Among the expected exotic properties of Majorana Kramers pairs are non-Abelian statistics¹⁵ and topological two-channel Kondo effect¹⁶.

The Kramers pair of Majorana modes has also been predicted to appear in TR-invariant vortex core of a TR-invariant topological superconductor¹⁰. TR transformation changes the parity of fermion number associated with the zero modes, and therefore acts as a supersymmetry in the vortex¹⁰. However, it remains unclear how a vortex defect that preserves TR symmetry can be physically realized, because a vortex in a superconductor is typically induced by a magnetic field that explicitly breaks TR symmetry. Here we propose that a TR-symmetric vortex naturally appears in a topological superconductor with nematic order. The nematic superconductor has a two-component order parameter¹⁷, which can be viewed as a planar vector. We demonstrate

analytically and numerically that a nematic vortex, such that only the vector part of the order parameter rotates, without $U(1)$ phase winding, is TR symmetric and binds a Majorana Kramers pair.

Our work is motivated by the recent experimental studies of superconducting *M*-doped Bi₂Se₃, where the metal element *M* can be Cu, Nb and Sr. Shortly after the experimental discovery of superconductivity in Cu_xBi₂Se₃¹⁸, Fu and Berg first proposed that a TR-invariant topological superconductor could be realized in this system¹¹. Majorana surface states associated with the topological superconductor were expected to be observable by point contact measurement¹⁹; however, scanning tunneling microscopy measurements²⁰ performed so far have not detected them. Despite the lack of observed surface states, measurements of bulk properties have revealed compelling evidence that the superconducting state in *M*_xBi₂Se₃ spontaneously breaks the lattice discrete rotational symmetry and therefore is nematic, and potentially topological. The main experimental evidence comes from the two-fold anisotropy of various bulk responses to an external magnetic field, including Knight shift²¹, specific heat²², upper critical field^{22,23} and magnetic torque²⁴. Corresponding theories of these bulk properties have also been developed^{25–28}.

Our paper is organized as follows. In Sec. II, we present the effective Hamiltonian²⁹ for the nematic odd-parity superconductor, and review its symmetry properties and gap structure. In Sec. III, we study electronic states in the continuous nematic vortex and provide an analytic solution to the Majorana Kramers pair. The zero modes can be understood in two different limits. In the limit of only helical *p*-wave pairing, spin up (down) electrons form $p_x + ip_y$ ($p_x - ip_y$) Cooper pair condensates. A nematic vortex thus exactly realizes a TR-symmetric vortex discussed in Ref. 10, where spin up and down electrons respectively experience a vortex and antivortex in the pairing order parameters. In the other limit of only polar *p*-wave pairing, the bulk of the superconductor is gapless. Surprisingly, we find that a single vortex can

induce a flat band of zero energy modes. A finite helical p -wave pairing potential lifts all the zero modes to finite energy except for one pair of Majorana modes. In Sec. IV, we study a discrete nematic vortex, which can be experimentally realized at the core where three nematic domains meet. In agreement with the analysis of continuous vortex, the discrete nematic vortex also binds a Kramers pair of Majorana modes. When the out-of-plane dispersion is included, the Majorana modes evolve into helical modes. Finally in Sec. V, we discuss possible ways to experimentally probe the zero modes in nematic vortex.

II. HAMILTONIAN AND SYMMETRY

Undoped Bi_2Se_3 is a strong topological insulator with both TR symmetry and inversion symmetry. Electronic bands in Bi_2Se_3 are therefore doubly degenerate at each \mathbf{k} point. For $M_x\text{Bi}_2\text{Se}_3$, we assume that the chemical potential lies in the conduction bands. When only the conduction bands near Γ point are retained in a low-energy theory, the superconducting state in $M_x\text{Bi}_2\text{Se}_3$ can be described by a one-orbital model^{11,29,30}:

$$\begin{aligned} H &= \frac{1}{2} \int dr \Psi_r^\dagger \mathcal{H}(\mathbf{k}) \Psi_r, \\ \Psi_r^\dagger &= (c_{r\uparrow}^\dagger, c_{r\downarrow}^\dagger, c_{r\downarrow}, -c_{r\uparrow}), \\ \mathcal{H}(\mathbf{k}) &= \mathcal{H}_0(\mathbf{k})\tau_z + \Delta(\mathbf{k})\tau_+ + \Delta^\dagger(\mathbf{k})\tau_-. \end{aligned} \quad (1)$$

Here \mathbf{k} is the three-dimensional momentum operator, and \uparrow and \downarrow are the pseudo-spin label of the two degenerate states in the conduction band. $\tau_\pm = (\tau_x \pm i\tau_y)/2$, and $\tau_{x,y,z}$ are Pauli matrices in Nambu space. \mathcal{H}_0 is the kinetic energy arising from band structure. We assume a parabolic dispersion: $\mathcal{H}_0(\mathbf{k}) = \beta\mathbf{k}^2 - \mu$, where $\mu > 0$ is the chemical potential. The nematic superconductor has an odd-parity pairing in the two-component E_u representation of the D_{3d} point group. The pairing potential can be expressed as:

$$\Delta(\mathbf{k}) = \boldsymbol{\eta} \cdot \mathbf{F}(\mathbf{k}), \quad (2)$$

where both $\boldsymbol{\eta}$ and \mathbf{F} represent a two-component vector. $\boldsymbol{\eta} = (\eta_x, \eta_y)$ acts as the nematic order parameter. \mathbf{F} can be decomposed into three parts when only linear \mathbf{k} terms are retained²⁹:

$$\begin{aligned} F_\alpha &= \lambda_1 F_\alpha^{(1)} + \lambda_2 F_\alpha^{(2)} + \lambda_3 F_\alpha^{(3)} \\ F_\alpha^{(1)} &= k_\alpha \sigma_z, & F_\alpha^{(3)} &= k_z \sigma_\alpha, \\ F_x^{(2)} &= k_x \sigma_y + k_y \sigma_x, & F_y^{(2)} &= k_x \sigma_x - k_y \sigma_y, \end{aligned} \quad (3)$$

where $\alpha = x, y$ and $F_{x,y}$ are the two components of \mathbf{F} . $\sigma_{x,y,z}$ are Pauli matrices in spin space. $\lambda_{1,2,3}$ are real parameters that characterize the relative strength of different pairing terms. When $\boldsymbol{\eta}$ is real, $\mathbf{F}^{(1)}$ and $\mathbf{F}^{(3)}$ represent polar p -wave pairing, and $\mathbf{F}^{(2)}$ is helical p -wave

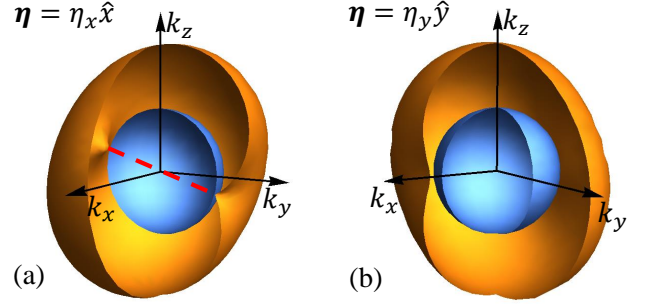


FIG. 1: Schematic gap structure (bronze color) on the Fermi surface (blue color). (a) $\boldsymbol{\eta} = \eta_x \hat{x}$. Red dashed line connects the two nodal points. (b) $\boldsymbol{\eta} = \eta_y \hat{y}$. There is a full superconductivity gap.

pairing where spin up (down) electrons respectively form $p_x + ip_y$ ($p_x - ip_y$) Cooper pairs.

We now elaborate on the symmetry properties when $\boldsymbol{\eta}$ is spatially uniform. The pairing potential has odd parity: $\Delta(-\mathbf{k}) = -\Delta(\mathbf{k})$. TR symmetry is preserved if $\boldsymbol{\eta}$ is real: $T\mathcal{H}(\mathbf{k})T^{-1} = \mathcal{H}(-\mathbf{k})$, where $T = -i\sigma_y K$ is the TR operator and K is the complex conjugate. The particle-hole (PH) symmetry can be expressed as: $\Xi\mathcal{H}(\mathbf{k})\Xi^{-1} = -\mathcal{H}(-\mathbf{k})$, where $\Xi = \sigma_y \tau_y K$.

The pairing potential Δ spontaneously breaks the three-fold rotational symmetry of Bi_2Se_3 . Rotating $\boldsymbol{\eta}$ by $2\pi/3$ leads to a different but energetically degenerate pairing potential. This is manifested by the following identity:

$$\Delta(\mathcal{R}_3\boldsymbol{\eta}, \mathcal{R}_3\mathbf{k}_\perp, k_z) = \mathcal{C}_3\Delta(\boldsymbol{\eta}, \mathbf{k}_\perp, k_z)\mathcal{C}_3^\dagger, \quad (4)$$

where $\mathbf{k}_\perp = (k_x, k_y)$ is the in-plane momentum. \mathcal{R}_3 is the real-space rotation matrix for a $2\pi/3$ rotation around z axis, and $\mathcal{C}_3 = \exp(-i\pi\sigma_z/3)$ is the rotation matrix in spin space.

In the D_{3d} point group there are three mirror planes that are located at $x = 0$ or its three-fold rotation counterparts. A mirror symmetry ($x \leftrightarrow -x$) is preserved if $\boldsymbol{\eta}$ is perpendicular to the corresponding mirror plane $x = 0$:

$$\begin{aligned} \Delta(\boldsymbol{\eta} = \eta_x \hat{x}, -k_x, k_y, k_z) \\ = \mathcal{M}\Delta(\boldsymbol{\eta} = \eta_x \hat{x}, k_x, k_y, k_z)\mathcal{M}^\dagger, \end{aligned} \quad (5)$$

where $\mathcal{M} = \exp(-i\pi\sigma_x/2)$ is the mirror operator in spin space. The superconductor has point nodes protected by the mirror symmetry when $\boldsymbol{\eta}$ is along \hat{x} ^{17,31,32}, as we discuss below.

As an odd-parity pairing potential, Δ can be expressed in terms of a vector \mathbf{d} :

$$\Delta(\mathbf{k}) = \mathbf{d}(\mathbf{k}) \cdot \boldsymbol{\sigma}. \quad (6)$$

When $\boldsymbol{\eta}$ is real, the superconductivity gap is given by $|\mathbf{d}(\mathbf{k})|$ on the Fermi surface³³. We present the explicit form of $\mathbf{d}(\mathbf{k})$ for two representative cases. In the case of $\boldsymbol{\eta} = \eta_x \hat{x}$,

$$\mathbf{d}(\mathbf{k}) = \eta_x(\lambda_2 k_y + \lambda_3 k_z, \lambda_2 k_x, \lambda_1 k_x). \quad (7)$$

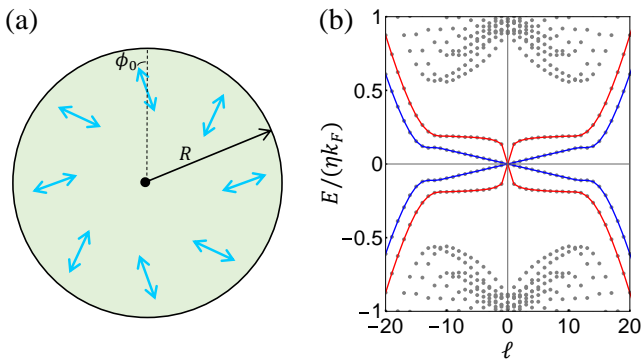


FIG. 2: (a) Illustration of a nematic vortex. The arrows indicate the orientation of the nematic order parameter $\boldsymbol{\eta}$. ϕ_0 describes the angle between $\boldsymbol{\eta}$ and the radial direction. We set ϕ_0 to be zero unless otherwise stated. (b) The energy spectrum of a gapped superconductor with a nematic vortex. The Hamiltonian is specified in (11). The calculation was performed for a disk with a radius $k_F R = 20$. To reduce computational cost, we used a large pairing potential $\eta k_F / \mu = 1$ for all numerical calculations in the paper. λ_1 and λ_2 are respectively taken to be 1 and 0.2. Red and blue lines respectively mark states localized near the core center and the outer edge of the disk. There are four modes that have nearly zero energy ($\sim 2 \times 10^{-5} \mu$) at $\ell = 0$. Proper linear combination of these four modes results in two states localized near the core, and another two states near the edge.

Because of the mirror symmetry in (5), $d_{y,z}$ vanishes on the mirror plane $k_x = 0$. Since \mathbf{d} is odd under inversion, $|\mathbf{d}(\mathbf{k})|$ must have nodes on the mirror plane. The point nodes are located at:

$$\mathbf{k} = \pm(0, \lambda_3, -\lambda_2)k_F / \sqrt{\lambda_3^2 + \lambda_2^2}, \quad (8)$$

where k_F is the Fermi wave vector $\sqrt{\mu/\beta}$. Note that the point nodes appear at non-zero k_z .

In another case $\boldsymbol{\eta} = \eta_y \hat{y}$,

$$\mathbf{d}(\mathbf{k}) = \eta_y (\lambda_2 k_x, -\lambda_2 k_y + \lambda_3 k_z, \lambda_1 k_y). \quad (9)$$

It is then impossible to make all three components of $\mathbf{d}(\mathbf{k})$ to vanish simultaneously on the Fermi surface, so the superconductor is fully gapped. The gap structures for the two different cases are schematically shown in Fig. 1. In summary, Hamiltonian (1) describes a topological Dirac superconductor³² with surface Majorana arcs when $\boldsymbol{\eta}$ is perpendicular to one of the mirror planes, and otherwise a fully gapped odd-parity topological superconductor¹¹.

III. CONTINUOUS NEMATIC VORTEX

Since the nematic superconductor has a two-component order parameter, a continuous vortex defect along \hat{z} is characterized by two winding numbers (n, m) :

$$\boldsymbol{\eta}(\mathbf{r}) = \eta(\rho) e^{in\phi} (\cos m\phi, \sin m\phi), \quad (10)$$

where (ρ, ϕ) are the polar coordinates of the in-plane position \mathbf{r}_\perp . The usual superconducting vortex has an integer phase winding number n and a zero value of m . n and m can also take half integer values: $(n, m) = (\pm 1/2, \pm 1/2)$, which correspond to half vortices³. Vortices with finite n break TR symmetry. In this paper, we focus on a TR-invariant vortex with $(n, m) = (0, 1)$, which we dub *nematic vortex*.

We study electronic states induced by the nematic vortex. As k_z remains a good quantum number, we start by considering $k_z = 0$. The dispersion of vortex states as a function of k_z will be discussed in Sec. IV. The Hamiltonian (1) at $k_z = 0$ and in the presence of nematic vortex can be expressed in polar coordinates as:

$$\begin{aligned} \tilde{\mathcal{H}} &= h_0 \tau_z + [\lambda_1 h_1 \sigma_z + \lambda_2 (h_2 \sigma_+ + h_2^\dagger \sigma_-)] \tau_x, \\ h_0 &\equiv \beta \mathbf{k}_\perp^2 - \mu = -\beta (\partial_\rho^2 + \frac{1}{\rho} \partial_\rho + \frac{1}{\rho^2} \partial_\phi^2) - \mu, \\ h_1 &\equiv (\boldsymbol{\eta} \cdot \mathbf{k} + \mathbf{k} \cdot \boldsymbol{\eta}) / 2 = -i\eta (\partial_\rho + \frac{1}{2\rho}), \\ h_2 &\equiv -i(\eta_+ k_+ + k_+ \eta_+) / 2 \\ &= -i\eta e^{i2\phi} [-i(\partial_\rho - \frac{1}{2\rho}) + \frac{\partial_\phi}{\rho}], \end{aligned} \quad (11)$$

where $\eta = |\boldsymbol{\eta}(\mathbf{r})|$, $k_\pm = k_x \pm ik_y$ and $\eta_\pm = \eta_x \pm i\eta_y$. In (11), the product between $\boldsymbol{\eta}$ and \mathbf{k} is symmetrized as they no longer commute when $\boldsymbol{\eta}$ has spatial variation. In the nematic vortex, η_+ and η_- respectively has a vortex $\exp(i\phi)$ and antivortex $\exp(-i\phi)$ structure. For the TR invariant vortex that we study, η_+ and η_- vanish at the same location in the vortex core. In the following we will neglect the spatial variation in $|\boldsymbol{\eta}(\mathbf{r})|$ to simplify calculation.

$\tilde{\mathcal{H}}$ preserves both TR and PH symmetries. Therefore, the nematic vortex described by (11) is in class DIII and can be characterized by a Z_2 invariant that signals the presence or absence of Majorana Kramers doublet in the vortex core³⁴. Here the existence of the zero modes is hinted by the limit in which h_1 term is absent in (11). In this limit, Hamiltonian (11) effectively describes a TR symmetric superconductor in which spin up and down electrons respectively form $p_x + ip_y$ and $p_x - ip_y$ Cooper pairs, and the superconducting phase has a vortex (antivortex) defect in the spin up (down) sector. Therefore, there must be a Kramers pair of Majorana modes when $\lambda_1 = 0$. By explicitly solving the eigenenergy problem of (11), we show that the zero modes are robust regardless of the exact values of $\lambda_{1,2}$.

Hamiltonian (11) has eigenvectors of the form:

$$e^{i\ell\phi} [e^{i\phi} f_1(\rho), e^{-i\phi} f_2(\rho), e^{i\phi} f_3(\rho), e^{-i\phi} f_4(\rho)]^T, \quad (12)$$

where ℓ takes integer values. For numerical diagonalization, $f_i(\rho)$ is expanded in terms of orthonormal Bessel functions on a finite-radius disk^{35,36}. The energy spectrum as a function of ℓ is illustrated in Fig. 2(b). The numerical results indicate that a pair of zero-energy modes with $\ell = 0$ are localized in the vortex core. Because of

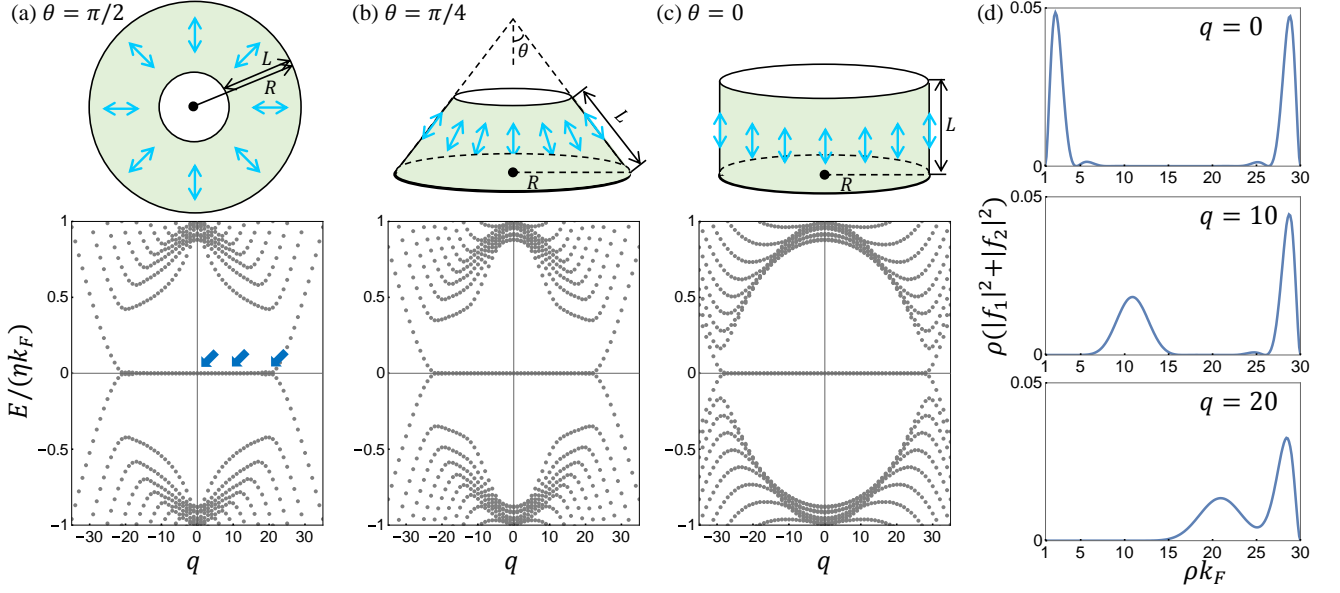


FIG. 3: (a)-(c) The lower panels show the energy spectrum of a polar p -wave superconductor ($\lambda_1 = 1, \lambda_2 = 0$) described by (15) in different geometries illustrated in the corresponding upper panel. (a) The nematic order parameter in the plane geometry ($\theta = \pi/2$) has a vortex structure. (b) When θ is less than $\pi/2$, Hamiltonian (15) can be viewed as defined on a truncated cone, where the radial coordinate ρ is measured from the tip of the cone. (c) When θ approaches 0, the truncated cone becomes a cylinder and the nematic order parameter becomes spatially uniform. Parameters R and L are kept fixed when θ varies: $k_F R = 30$ and $k_F L = 29$. (d) Real space probability distribution of states that have an energy slightly above zero at $q = 0, 10$ and 20 in the plane geometry ($\theta = \pi/2$). The states are indicated by the blue arrows in (a).

PH and TR symmetries, they must be Majorana modes and TR partners:

$$\begin{aligned} \gamma_{\uparrow}^{\dagger} &= \int d\mathbf{r} [(e^{i\phi} \xi_1(\rho) c_{r\uparrow}^{\dagger} + e^{-i\phi} \xi_2(\rho) c_{r\downarrow}^{\dagger}) + h.c.], \\ \gamma_{\downarrow}^{\dagger} &= \int d\mathbf{r} [(-e^{i\phi} \xi_2^*(\rho) c_{r\uparrow}^{\dagger} + e^{-i\phi} \xi_1^*(\rho) c_{r\downarrow}^{\dagger}) + h.c.], \end{aligned} \quad (13)$$

which satisfy the Majorana condition ($\gamma_{\uparrow,\downarrow}^{\dagger} = \gamma_{\uparrow,\downarrow}$) and form Kramers doublet under TR transformation ($\gamma_{\uparrow} \rightarrow \gamma_{\downarrow}, \gamma_{\downarrow} \rightarrow -\gamma_{\uparrow}$). As shown in Appendix A, wave functions $\xi_{1,2}$ can be obtained analytically:

$$\begin{aligned} [\xi_1, \xi_2] &= [i(\lambda_2 + \sqrt{\lambda_1^2 + \lambda_2^2}), \lambda_1] \xi, \\ \xi(\rho) &= \mathcal{N} J_1(\sqrt{1 - (\tilde{\eta} k_F / 2\mu)^2} k_F \rho) \exp(-\frac{\tilde{\eta}}{2\beta} \rho), \end{aligned} \quad (14)$$

where \mathcal{N} represents a normalization factor and J_1 is Bessel function of the first order. In (14), $\lambda_{1,2} \geq 0$ is assumed, and $\tilde{\eta}$ is the effective total pairing strength $\eta \sqrt{\lambda_1^2 + \lambda_2^2}$.

We analyze (14) in two different limits. In the limit $\lambda_1 = 0$, ξ_2 vanishes and $\gamma_{\uparrow,\downarrow}^{\dagger}$ is the Majorana mode in corresponding spin sector, as expected. In the other limit $\lambda_2 = 0$, the zero modes are also exponentially confined to the vortex center. This result is surprising, since the Hamiltonian (1) with zero λ_2 describes a *gapless* polar p -wave superconductor. Next we reveal another unexpected effect – that the polar p -wave superconductor sup-

ports not just one pair, but a flat band of zero modes localized around the nematic vortex core, despite the bulk being gapless.

Hamiltonian (1) with $k_z = 0$ and $\lambda_2 = 0$ reduces to

$$H_1 = \int d\mathbf{r} (c_{r\uparrow}^{\dagger}, c_{r\downarrow}) \mathcal{H}_1 \begin{pmatrix} c_{r\uparrow} \\ c_{r\downarrow}^{\dagger} \end{pmatrix}, \quad \mathcal{H}_1 = h_0 \tau_z + \lambda_1 h_1 \tau_x, \quad (15)$$

where $h_{0,1}$ is provided in (11). We reiterate their expressions below but introduce a new parameter θ that can be used to tune the system geometry,

$$\begin{aligned} h_0 &\equiv \beta \mathbf{k}_{\perp}^2 - \mu = -\beta (\partial_{\rho}^2 + \frac{1}{\rho} \partial_{\rho} + \frac{1}{\rho^2 \sin^2 \theta} \partial_{\phi}^2) - \mu, \\ h_1 &\equiv (\boldsymbol{\eta} \cdot \mathbf{k} + \mathbf{k} \cdot \boldsymbol{\eta}) / 2 = -i\eta (\partial_{\rho} + \frac{1}{2\rho}). \end{aligned} \quad (16)$$

$\theta = \pi/2$ corresponds to a flat plane geometry. When $\theta < \pi/2$, Eq. (16) generalizes the problem on a plane to a cone with an opening angle 2θ , as illustrated in Fig. 3. This generalization is derived in Appendix B and is used to shed light on relationship between the vortex core states and edge modes in cylindrical geometry.

Similar to $\tilde{\mathcal{H}}$ in (11), the operator \mathcal{H}_1 in (16) has eigenstates of the form

$$\exp(iq\phi) [f_1(\rho), f_2(\rho)]^T, \quad (17)$$

where q is an integer. We solve (15) and (16) in the

following range of ρ ,

$$\frac{R}{\sin \theta} - L < \rho < \frac{R}{\sin \theta}, \quad (18)$$

with open boundary conditions. This specifies an annulus in the plane when $\theta = \pi/2$ and a truncated cone with a base radius R when $\theta < \pi/2$.

An important special case is $\theta \rightarrow 0$. In this limit, $\rho \rightarrow \infty$, while $\rho \sin \theta$ stays at a finite value R . Geometrically, the truncated cone becomes a cylinder with a radius R and a finite length L . Eq. (16) then describes exactly a *uniform* polar p -wave superconductor on the cylinder, as depicted in Fig. 3(c). It is known that a polar p -wave superconductor supports a flat band of zero-energy modes confined to edges³⁷.

Equations (16) and (18) state that the polar p -wave superconductor with a nematic vortex in the annular geometry can be related to a *uniform* one on the cylinder via a single parameter θ . We solved the eigenvalue problem for different θ values using the ansatz (17). The energy spectrum as a function of q is shown in Fig. 3. The zero-energy modes with small $|q|$ index on cylinder ($\theta = 0$) remain at zero as θ increases, all the way to $\theta = \pi/2$.

Because of a PH symmetry of \mathcal{H}_1 ($\tau_y \mathcal{H}_1 = -\mathcal{H}_1 \tau_y$), the zero modes are eigenstates of τ_y . Therefore the q th zero mode localized near the inner edge can be parametrized as:

$$d_q^\dagger = \int dr e^{iq\phi} \psi_q(\rho) [i c_{r\uparrow}^\dagger + c_{r\downarrow}], \quad (19)$$

where $\psi_q(\rho)$ is the radial part of the wave function. The degree of confinement of $\psi_q(\rho)$ to the inner edge depends on the index q , as illustrated in Fig. 3(d). $\psi_q(\rho)$ moves away from the inner edge as $|q|$ increases due to a ‘‘centrifugal force’’ in (16). In the annulus geometry ($\theta = \pi/2$), the zero modes are robust when the inner radius becomes zero ($L \rightarrow R$). As shown in Appendix C, an analytic solution of the wave function $\psi_q(\rho)$ can be obtained at every integer q for a disk with an infinite radius. The number of zero modes becomes finite on a finite-radius disk due to hybridization between modes deriving from the core and the outer edge. The stability of the flat band with respect to disorder and interactions is an interesting topic, beyond the scope of this paper. Previous work on related problems can be found, for example, in Ref 38–40.

Starting from the polar phase, we can examine the effect of the helical part of the pairing potential $\lambda_2(\boldsymbol{\eta} \cdot \mathbf{F}^{(2)} + \mathbf{F}^{(2)} \cdot \boldsymbol{\eta})/2$ by including it as a perturbation, and projecting it onto the zero modes d_q^\dagger . The projection leads to the following effective low energy Hamiltonian:

$$\tilde{H}_2 = \lambda_2 \sum_{p>0} \varepsilon_p d_{1+p}^\dagger d_{1-p}^\dagger + \varepsilon_p^* d_{1-p} d_{1+p}, \quad (20)$$

where $p = 0$ term is absent because of fermion anticommutation relation. Therefore, all zero modes except d_1^\dagger

are lifted to finite energy when $\lambda_2 \neq 0$. d_1^\dagger can be decomposed into two Majorana modes:

$$\gamma_\uparrow^\dagger = d_1^\dagger + d_1, \gamma_\downarrow^\dagger = i(d_1^\dagger - d_1), \quad (21)$$

which are exactly those presented in (13). As a summary, the Majorana Kramers doublet $\gamma_{\uparrow,\downarrow}^\dagger$ can be understood either from the helical limit $\lambda_1 = 0$ or the polar limit $\lambda_2 = 0$.

The degeneracy between γ_\uparrow^\dagger and $\gamma_\downarrow^\dagger$ is protected by TR symmetry. TR changes the fermion parity associated with fermion mode d_1 and acts as: $d_1^\dagger \rightarrow -id_1$ and $d_1 \rightarrow id_1^\dagger$, which is a manifestation of supersymmetry. A mass term $d_1^\dagger d_1$ is prohibited by TR symmetry. When TR symmetry is explicitly broken, for example by a Zeeman term of the form $\varepsilon_z \sigma_z$, generally there can be coupling between γ_\uparrow^\dagger and $\gamma_\downarrow^\dagger$ that lifts the degeneracy.

IV. DISCRETE NEMATIC VORTEX

Because Bi_2Se_3 only has a discrete three-fold rotational symmetry, the nematic vector $\boldsymbol{\eta}$ is expected to be pinned to one of the high symmetry directions. The Ginzburg-Landau free energy for a uniform state is¹⁷:

$$\mathcal{F} = b_0(|\eta_x|^2 + |\eta_y|^2) + b_1(|\eta_x|^2 + |\eta_y|^2)^2 + b_2(\eta_x^2 + \eta_y^2)^2 + b_3[(\eta_+^* \eta_-)^3 + (\eta_-^* \eta_+)^3]. \quad (22)$$

Here the sign of b_2 distinguishes between nematic and chiral states, which have respectively real and complex order parameters $\boldsymbol{\eta}$. We assume $b_2 < 0$ so that a nematic state is energetically favorable. The sixth-order terms in \mathcal{F} capture the crystalline anisotropy. The sign of b_3 determines whether $\boldsymbol{\eta}$ is pinned to be perpendicular or parallel to one of the three mirror planes, for example, along x or y direction. Because of the lattice anisotropy, a continuous nematic vortex described by (10) is energetically unfavorable. Nevertheless, a discrete vortex can be realized around the core where three nematic domains meet, as illustrated in Fig. 4. Indeed, a recent experiment on the specific heat of $\text{Cu}_x\text{Bi}_2\text{Se}_3$ under magnetic field has indicated the existence of multiple nematic domain walls within one sample²². Therefore, a discrete nematic vortex may naturally appear due to local disorder or strain effects.

To numerically study the discrete vortex, we regularize the Hamiltonian (1) on a triangular lattice. Two representative types of discrete vortex are studied. In type I, $\boldsymbol{\eta}$ within each domain is parallel to a mirror plane. The bulk of each domain is therefore fully gapped, as illustrated in Fig. 1(b). The numerical calculation for $k_z = 0$ indicates that there are four zero modes. Two of them are localized around the core center and the other two are bound to edges[see Fig. 4(a)], which are expected from the analysis of the continuous vortex. At finite k_z , the two zero modes localized around the core evolve into two branches that disperse linearly with k_z as shown in

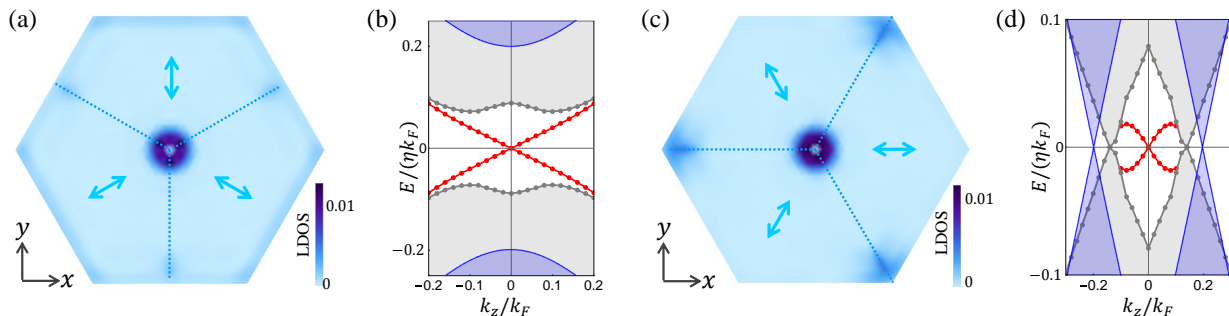


FIG. 4: (a) and (b) Type I discrete nematic vortex. (a) Real space local density of states (LDOS) corresponding to one of the four modes at $k_z = 0$ that have nearly zero energy ($\sim 5 \times 10^{-4}\mu$). The three dashed lines mark the boundaries between different nematic domains, which also coincide with the three mirror planes. The nematic order parameter is uniform within each domain and its direction is illustrated by the arrow. (b) The red lines indicate the k_z dispersion of states localized near the core center. The shaded region illustrates the bulk excitation continuum. The blue lines show the minimum energy excitation of a *uniform* state with η along y direction. Parameter values are $(\lambda_1, \lambda_3, \lambda_2) = (1, 1, 0.2)$. (c) and (d) Corresponding plots for type II discrete nematic vortex. In (d) the blue lines show the minimum energy excitation of a *uniform* state with η along x direction.

Fig. 4(b) and therefore can be identified as helical Majorana modes.

In type II, η within each domain is perpendicular to a mirror plane. The bulk of each domain in this case is gapless, and the point nodes are at $k_z \neq 0$, as shown in Fig. 1(a). There are still two zero modes localized around the core for $k_z = 0$, at which the bulk is fully gapped. At finite k_z , the helical modes merge into the bulk excitation continuum. The bulk excitations of the discrete vortex structure become gapless at a finite k_z (Fig. 4(d)). The exact values of k_z where the bulk excitation minimum are located are slightly different for the domain structure and the uniform state due to the presence of domain core and finite size effects. As k_z may not be conserved in the presence of disorder, the zero modes in type II vortex are not as robust as those in type I.

The energy cost of a domain wall scales linearly with the area of the interface between two domains. This energy cost could be remedied by studying a sample with mesoscopic geometries⁴¹. Another possibility that discrete vortices could be stabilized is due to Imry-Ma scenario⁴², as the nematic order parameter can couple to local disorder or strain field¹⁷.

V. DISCUSSION

The presence of the Majorana Kramers pair will lead to an enhanced density of states (DOS) near the vortex core at zero energy. To probe the enhanced DOS, it would be favorable to study materials in a thin film geometry so that the motion along z is quantized. Scanning tunneling microscope (STM) is particularly suitable to search for the zero modes. STM has been successfully used to detect Majorana modes in different schemes^{9,43}, and to identify nematic states in the quantum Hall regime⁴⁴. Within each nematic domain of $M_x\text{Bi}_2\text{Se}_3$, the nematic order

parameter will lead to a two-fold anisotropy in electronic band structure, which should be detectable in quasiparticle interference pattern in STM⁴⁵⁻⁴⁷. Different nematic domains will have different interference pattern, and thus can also be distinguished.

In summary, a nematic vortex can be realized in odd-parity topological superconductors. It is an unusual type of topological defect that preserves time reversal symmetry and binds a Kramers pair of Majorana modes. Other interesting properties of nematic odd-parity topological superconductors are likely to await discovery.

VI. ACKNOWLEDGMENT

We acknowledge support from Department of Energy, Office of Basic Energy Science, Materials Science and Engineering Division.

Appendix A: Analytic solution to zero modes in nematic vortex

In this appendix, we present the details of obtaining analytic solution to Majorana zero modes. Equation (13) is an ansatz to zero modes of Hamiltonian (11). Wave functions $\xi_{1,2}$ satisfy the following equations:

$$\begin{aligned} \tilde{h}_0 \xi_1 + \lambda_1 h_1 \xi_2^* - \lambda_2 \tilde{h}_2 \xi_1^* &= 0, \\ \tilde{h}_0 \xi_2^* - \lambda_1 h_1 \xi_1 - \lambda_2 \tilde{h}_2 \xi_2 &= 0, \end{aligned} \quad (\text{A1})$$

where \tilde{h}_0 and \tilde{h}_2 are given by:

$$\begin{aligned} \tilde{h}_0 &= e^{-i\phi} h_0 e^{i\phi} = -\beta (\partial_\rho^2 + \frac{1}{\rho} \partial_\rho - \frac{1}{\rho^2}) - \mu, \\ \tilde{h}_2 &= e^{-i\phi} h_2 e^{-i\phi} = -\eta (\partial_\rho + \frac{1}{2\rho}). \end{aligned} \quad (\text{A2})$$

It is important to note that $h_1 = i\tilde{h}_2$, which makes analytic solution possible. Equation (A1) reduces to:

$$\begin{aligned}\tilde{h}_0\xi_1 + \tilde{h}_2(i\lambda_1\xi_2^* - \lambda_2\xi_1^*) &= 0, \\ \tilde{h}_0\xi_2^* - \tilde{h}_2(i\lambda_1\xi_1 + \lambda_2\xi_2) &= 0.\end{aligned}\quad (\text{A3})$$

To proceed we make the following ansatz:

$$\begin{aligned}(\xi_1, \xi_2) &= (u, v)\xi, \\ \xi &= \mathcal{N}J_1(\sqrt{1 - (\Lambda\eta k_F/2\mu)^2}k_F\rho) \exp(-\frac{\Lambda\eta}{2\beta}\rho),\end{aligned}\quad (\text{A4})$$

where u , v and Λ are parameters that need to be determined. \mathcal{N} is just a normalization factor. Ansatz in (A4) is proposed based on the following identity:

$$(\tilde{h}_0 + \Lambda\tilde{h}_2)\xi = 0. \quad (\text{A5})$$

Equation (A3) then simplifies to an algebraic equation:

$$\begin{aligned}-\Lambda u + i\lambda_1 v^* - \lambda_2 u^* &= 0, \\ \Lambda v^* + i\lambda_1 u + \lambda_2 v &= 0.\end{aligned}\quad (\text{A6})$$

When u and v are decomposed into their real and imaginary parts, equation (A6) can be viewed as an eigenproblem with Λ as the eigenvalue. There are two eigenvalues $\pm\sqrt{\lambda_1^2 + \lambda_2^2}$. We choose $\Lambda = \sqrt{\lambda_1^2 + \lambda_2^2}$ so that the zero modes are exponentially confined to the center. Given $\Lambda = \sqrt{\lambda_1^2 + \lambda_2^2}$, there are two solutions for (u, v) :

$$\begin{aligned}(u_1, v_1) &= [i(\lambda_2 + \sqrt{\lambda_1^2 + \lambda_2^2}), \lambda_1], \\ (u_2, v_2) &= (-v_1, u_1^*),\end{aligned}\quad (\text{A7})$$

where $\lambda_{1,2} \geq 0$ is assumed without loss of generality. (u_1, v_1) leads to the solution in (14). (u_2, v_2) does not give rise to an independent solution but just switches the definition of $\gamma_{\uparrow}^{\dagger}$ and $\gamma_{\downarrow}^{\dagger}$.

Appendix B: Cone geometry

In this appendix, we present some mathematical properties on the cone geometry. The coordinate on a cone is (ρ, ϕ) , where ρ is the radial coordinate measured from the tip of the cone, and ϕ is the azimuthal angle. The gradient and Laplace operators on the cone are

$$\begin{aligned}\nabla &= \partial_{\rho}\hat{\rho} + \frac{1}{\rho\sin\theta}\partial_{\phi}\hat{\phi}, \\ \nabla^2 &= \partial_{\rho}^2 + \frac{1}{\rho}\partial_{\rho} + \frac{1}{\rho^2\sin^2\theta}\partial_{\phi}^2,\end{aligned}\quad (\text{B1})$$

where $\hat{\rho}$ and $\hat{\phi}$ are respectively the unit vectors along the radial and the azimuthal direction. θ is half of the opening angle of the cone, as shown in Fig. 3(b). The following identities are used to derive the Laplace operator from the gradient operator:

$$\partial_{\rho}\hat{\phi} = 0, \quad \partial_{\phi}\hat{\rho} = \sin\theta\hat{\phi}. \quad (\text{B2})$$

We now show how the Hamiltonian in (15) and (16) are derived on the cone geometry. The kinetic energy has a simple connection to the Laplace operator: $h_0 = \beta k_{\perp}^2 - \mu = -\beta\nabla^2 - \mu$. The pairing order parameter $\boldsymbol{\eta}$ varies in space in the following way:

$$\boldsymbol{\eta} = \eta(\cos\phi_0\hat{\rho} + \sin\phi_0\hat{\phi}), \quad (\text{B3})$$

where ϕ_0 is the angle between the order parameter $\boldsymbol{\eta}$ and the radial direction. In the main text, we have set $\phi_0 = 0$. h_1 has the expression:

$$\begin{aligned}h_1 &= -i(\boldsymbol{\eta} \cdot \nabla + \nabla \cdot \boldsymbol{\eta})/2 \\ &= -i(\eta\cos\phi_0)(\partial_{\rho} + \frac{1}{2\rho}) - i\frac{\eta\sin\phi_0}{\rho\sin\theta}\partial_{\phi}.\end{aligned}\quad (\text{B4})$$

When $\phi_0 = 0$, the nematic order parameter $\boldsymbol{\eta}$ is parallel to the radial direction, providing a confinement potential. As ϕ_0 increases, the confinement along radial direction becomes weaker. In the special case of $\phi_0 = \pi/2$, the confinement is completely lost and there are no zero-energy modes. Therefore, the presence of zero modes in the nematic vortex of a polar p -wave superconductor requires that ϕ_0 is not $\pi/2$.

Finally, the orthonormal basis functions on the truncated cone are:

$$f_{q,j}(\rho, \phi) = \frac{e^{iq\phi}}{\sqrt{2\pi}} \times \sqrt{\frac{2}{L}} \frac{\sin\frac{j\pi}{L}(\rho - \frac{R}{\sin\theta} + L)}{\sqrt{\sin\theta\rho}}, \quad (\text{B5})$$

where q and j are integer numbers. $f_{q,j}$ vanishes at the two edges of the truncated cone. The energy spectrum on the cone geometry is obtained by expanding wave functions in terms of $f_{q,j}$.

Appendix C: Analytic solution to the flat band of zero modes

In this appendix, we present analytic solutions to the flat band of zero modes in the nematic vortex of a polar p -wave superconductor. Here we consider a disk geometry with no hole ($L = R$) and an infinite radius ($R \rightarrow +\infty$). The q th zero modes centered around the origin is presented in (19). The wave function $\psi_q(\rho)$ satisfies the following equation:

$$[\beta(\partial_{\rho}^2 + \frac{1}{\rho}\partial_{\rho} - \frac{q^2}{\rho^2}) + \mu + \lambda_1\eta(\partial_{\rho} + \frac{1}{2\rho})]\psi_q(\rho) = 0, \quad (\text{C1})$$

which has the analytic solution

$$\psi_q(\rho) = \mathcal{N}J_q(\sqrt{1 - (\lambda_1\eta k_F/2\mu)^2}k_F\rho) \exp(-\frac{\lambda_1\eta}{2\beta}\rho), \quad (\text{C2})$$

where J_q is the q th Bessel function. It is interesting to note that there is a zero-energy solution for every integer q on the disk with infinite radius. As $|q|$ increases, $\psi_q(\rho)$ moves away from the origin. On a finite-radius disk, there are also zero modes bound to the outer edge, which can

hybridize with $\psi_q(\rho)$ if the latter has a significant probability near the outer edge. Therefore, the number of zero modes on a finite-radius disk is finite, but it increases as R increases.

To gain a deeper insight, we revisit the problem of a superconducting vortex with an odd winding number in a polar p -wave superconductor⁴⁸. The effective Hamiltonian is:

$$H_q = (\beta k^2 - \mu)\tau_z + \left[\frac{1}{2}(\kappa k_- + k_- \kappa)\tau_+ + h.c.\right], \quad (C3)$$

where $\kappa = \eta \exp[i(2q+1)\phi]$ represents the vortex with winding number $2q+1$, where q is an integer. In polar coordinates, we have:

$$\frac{1}{2}(\kappa k_- + k_- \kappa) = \eta e^{i2q\phi} \left[-i(\partial_\rho + \frac{2q+1}{2\rho}) - \frac{\partial_\phi}{\rho} \right]. \quad (C4)$$

It is known that H_q supports one zero energy mode⁴⁸. We look for zero mode of the following form:

$$[ie^{iq\phi}, e^{-iq\phi}]^T \psi_q(\rho). \quad (C5)$$

Here the wave function $\psi_q(\rho)$ should satisfy

$$\left[\beta(\partial_\rho^2 + \frac{1}{\rho}\partial_\rho - \frac{q^2}{\rho^2}) + \mu + \eta(\partial_\rho + \frac{1}{2\rho}) \right] \psi_q(\rho) = 0, \quad (C6)$$

which shares exactly the same form as (C1). This provides another point of view on the reason why a polar p -wave superconductor supports a flat band of zero modes in the presence of a nematic vortex.

-
- ¹ A. Y. Kitaev, *Physics-Uspekhi* **44**, 131 (2001).
² N. Read and D. Green, *Phys. Rev. B* **61**, 10267 (2000).
³ D. A. Ivanov, *Phys. Rev. Lett.* **86**, 268 (2001).
⁴ A. Y. Kitaev, *Annals of Physics* **303**, 2 (2003).
⁵ L. Fu and C. L. Kane, *Phys. Rev. Lett.* **100**, 096407 (2008).
⁶ J. D. Sau, R. M. Lutchyn, S. Tewari, and S. Das Sarma, *Phys. Rev. Lett.* **104**, 040502 (2010).
⁷ R. M. Lutchyn, J. D. Sau, and S. Das Sarma, *Phys. Rev. Lett.* **105**, 077001 (2010).
⁸ S. M. Albrecht, A. Higginbotham, M. Madsen, F. Kuemmeth, T. S. Jespersen, J. Nygård, P. Krogstrup, and C. Marcus, *Nature* **531**, 206 (2016).
⁹ H.-H. Sun, K.-W. Zhang, L.-H. Hu, C. Li, G.-Y. Wang, H.-Y. Ma, Z.-A. Xu, C.-L. Gao, D.-D. Guan, Y.-Y. Li, C. Liu, D. Qian, Y. Zhou, L. Fu, S.-C. Li, F.-C. Zhang, and J.-F. Jia, *Phys. Rev. Lett.* **116**, 257003 (2016).
¹⁰ X.-L. Qi, T. L. Hughes, S. Raghu, and S.-C. Zhang, *Phys. Rev. Lett.* **102**, 187001 (2009).
¹¹ L. Fu and E. Berg, *Phys. Rev. Lett.* **105**, 097001 (2010).
¹² A. Keselman, L. Fu, A. Stern, and E. Berg, *Phys. Rev. Lett.* **111**, 116402 (2013).
¹³ C. Schrade, A. A. Zyuzin, J. Klinovaja, and D. Loss, *Phys. Rev. Lett.* **115**, 237001 (2015).
¹⁴ F. Zhang, C. L. Kane, and E. J. Mele, *Phys. Rev. Lett.* **111**, 056402 (2013).
¹⁵ X.-J. Liu, C. L. M. Wong, and K. T. Law, *Phys. Rev. X* **4**, 021018 (2014).
¹⁶ Z.-q. Bao and F. Zhang, arXiv:1607.04303 (2016).
¹⁷ L. Fu, *Phys. Rev. B* **90**, 100509 (2014).
¹⁸ Y. S. Hor, A. J. Williams, J. G. Checkelsky, P. Roushan, J. Seo, Q. Xu, H. W. Zandbergen, A. Yazdani, N. P. Ong, and R. J. Cava, *Phys. Rev. Lett.* **104**, 057001 (2010).
¹⁹ S. Sasaki, M. Kriener, K. Segawa, K. Yada, Y. Tanaka, M. Sato, and Y. Ando, *Phys. Rev. Lett.* **107**, 217001 (2011).
²⁰ N. Levy, T. Zhang, J. Ha, F. Sharifi, A. A. Talin, Y. Kuk, and J. A. Stroscio, *Phys. Rev. Lett.* **110**, 117001 (2013).
²¹ K. Matano, M. Kriener, K. Segawa, Y. Ando, and G.-q. Zheng, *Nat. Phys.* **12**, 852 (2016).
²² S. Yonezawa, K. Tajiri, S. Nakata, Y. Nagai, Z. Wang, K. Segawa, Y. Ando, and Y. Maeno, *Nat. Phys.* **13**, 123 (2017).
²³ Y. Pan, A. Nikitin, G. Araizi, Y. Huang, Y. Matsushita, T. Naka, and A. De Visser, *Sci. Rep.* **6**, 28632 (2016).
²⁴ T. Asaba, B. J. Lawson, C. Tinsman, L. Chen, P. Corbae, G. Li, Y. Qiu, Y. S. Hor, L. Fu, and L. Li, *Phys. Rev. X* **7**, 011009 (2017).
²⁵ T. Hashimoto, K. Yada, A. Yamakage, M. Sato, and Y. Tanaka, *J. Phys. Soc. Jpn.* **82**, 044704 (2013).
²⁶ Y. Nagai and Y. Ota, *Phys. Rev. B* **94**, 134516 (2016).
²⁷ J. W. F. Venderbos, V. Kozii, and L. Fu, *Phys. Rev. B* **94**, 094522 (2016).
²⁸ V. Kozii, J. W. Venderbos, and L. Fu, *Sci. Adv.* **2**, e1601835 (2016).
²⁹ J. W. F. Venderbos, V. Kozii, and L. Fu, *Phys. Rev. B* **94**, 180504 (2016).
³⁰ S.-K. Yip, *Phys. Rev. B* **87**, 104505 (2013).
³¹ F. Zhang, C. L. Kane, and E. J. Mele, *Phys. Rev. Lett.* **111**, 056403 (2013).
³² S. A. Yang, H. Pan, and F. Zhang, *Phys. Rev. Lett.* **113**, 046401 (2014).
³³ M. Sigrist and K. Ueda, *Rev. Mod. Phys.* **63**, 239 (1991).
³⁴ J. C. Y. Teo and C. L. Kane, *Phys. Rev. B* **82**, 115120 (2010).
³⁵ F. Gygi and M. Schlüter, *Phys. Rev. B* **43**, 7609 (1991).
³⁶ T. Kawakami and X. Hu, *Phys. Rev. Lett.* **115**, 177001 (2015).
³⁷ I. Martin and A. F. Morpurgo, *Phys. Rev. B* **85**, 144505 (2012).
³⁸ Y. Li, D. Wang, and C. Wu, *New Journal of Physics* **15**, 085002 (2013).
³⁹ A. C. Potter and P. A. Lee, *Phys. Rev. Lett.* **112**, 117002 (2014).
⁴⁰ Y. Baum, T. Posske, I. C. Fulga, B. Trauzettel, and A. Stern, *Phys. Rev. Lett.* **114**, 136801 (2015).
⁴¹ S. B. Chung, H. Bluhm, and E.-A. Kim, *Phys. Rev. Lett.* **99**, 197002 (2007).
⁴² Y. Imry and S.-k. Ma, *Phys. Rev. Lett.* **35**, 1399 (1975).
⁴³ S. Nadj-Perge, I. K. Drozdov, J. Li, H. Chen, S. Jeon, J. Seo, A. H. MacDonald, B. A. Bernevig, and A. Yazdani, *Science* **346**, 602 (2014).
⁴⁴ B. E. Feldman, M. T. Randeria, A. Gyenis, F. Wu, H. Ji,

- R. Cava, A. H. MacDonald, and A. Yazdani, *Science* **354**, 316 (2016).
- ⁴⁵ J. S. Hofmann, R. Queiroz, and A. P. Schnyder, *Phys. Rev. B* **88**, 134505 (2013).
- ⁴⁶ A. Farrell, M. Beaudry, M. Franz, and T. Pereg-Barnea, *Phys. Rev. B* **91**, 134510 (2015).
- ⁴⁷ F. Lambert, A. Akbari., P. Thalmeier, and I. Eremin, *Phys. Rev. Lett.* **118**, 087004 (2017).
- ⁴⁸ G. Volovik, *JETP Letters* **70**, 609 (1999).